Inertia-induced coherent structures in a time-periodic viscous flow

Inertia-induced coherent structures in a time-periodic viscous mixing flow

M. F. M. Speetjens,[a] H. J. H. Clercx, and G. J. F. van Heijst
Fluid Dynamics Laboratory, Department of Physics, Eindhoven University of Technology, P.O. Box 513, 5600 MB Eindhoven, The Netherlands

(Received 2 February 2006; accepted 3 August 2006; published online 29 August 2006)

Inertia-induced changes in transport properties of an incompressible viscous time-periodic flow due to fluid inertia (nonzero Reynolds numbers Re) are studied in terms of the topological properties of volume-preserving maps. In the noninertial Stokes limit (vanishing Re), the flow relates to a so-called one-action map. However, the corresponding invariant surfaces are topologically equivalent to spheres rather than the common case of tori. This has fundamental ramifications for the response to small departures from the noninertial limit and leads to a new type of response scenario: resonance-induced merger of coherent structures. Thus several coexisting families of two-dimensional coherent structures are formed that make up two classes: fully closed structures and leaky structures. Fully closed structures restrict motion as in a one-action map; leaky structures have open boundaries that connect with a locally chaotic region through which exchange of material with other leaky structures occurs. For large departures from the noninertial limit the above structures vanish and the topology becomes determined by isolated periodic points and associated manifolds. This results in unrestricted chaotic motion. © *2006 American Institute of Physics*. [DOI: 10.1063/1.2345208]

I. INTRODUCTION

Mixing of fluids by three-dimensional (3D) time-periodic laminar flows ("viscous mixing") is an important element of many physical processes in nature and in industry. Consider for instance the periodic melt extraction from magma chambers in the Earth's mantle[1] and food and industrial mixing devices in process technology employing time-periodic fluid agitation.[2] However, despite the omnipresence of viscous mixing, to date, still a poor understanding exists of the underlying mechanisms.[2–5] The study hereafter is motivated by this and aims to contribute to the present knowledge on viscous mixing via the analysis of a realistic and prototypical model problem.

The presented analysis examines viscous mixing in terms of the 3D advection of passive tracers in time-periodic flows. Such flows admit reduction to volume-preserving maps classified by the number of constants of motion ("actions") they may possess.[6] Three kinds of maps can be distinguished: zero-, one-, and two-action maps.[7] One-action and two-action maps confine tracers to dense sets of invariant surfaces and curves, respectively, that impede unrestricted advection and thus imply inefficient mixing; zero-action maps are devoid of geometrical constraints and admit the unrestricted (chaotic) advection that is key to efficient mixing. Attainment of efficient mixing is in the current framework thus synonymous to the destruction of the transport barriers of the one-action and two-action maps, effectively transforming them into zero-action maps, through perturbation by, for instance, inertia.

Weak perturbation of two-action maps causes coalescence of invariant curves into surfaces and thus strictly transforms them into one-action maps.[6] These invariant surfaces may develop local defects, though, that enable global advection via the mechanism of resonance-induced dispersion (RID).[6,8–12] The intact sections of the invariant surfaces nonetheless determine the tracer transport significantly by restricting motion outside these defects, making this dispersion process an extremely slow one, suggesting the perturbed system, though essentially a zero-action map, still behaves very much like a one-action map. Perturbation strengths increasingly beyond this state progressively destroy the remnants of the invariant surfaces and the map approaches a truly zero-action state. In-depth studies on the actual changes undergone by the topology during this transition appear nonexistent, though. Perturbation of one-action maps with invariant tori gives the "classical" Hamiltonian scenario: Kolmogorov-Arnold-Moser (KAM)-like survival of nonresonant tori and Poincaré-Birkhoff-like breakup of resonant tori.[6,11–13] Surviving tori progressively disintegrate with increasing perturbation until at some finite departure from the unperturbed state the invariant tori have vanished completely and the system has transformed into a zero-action state.[14] However, this particular progression from the one-action state to the globally chaotic zero-action state with increasing perturbation strength holds only in the specific case of invariant surfaces topologically equivalent to tori. Response scenarios for invariant surfaces other than tori is an important aspect that appears unexplored to date. Further aspects unexplored are the role of intrasurface chaos in response scenarios of one-action maps[15] and the topology of the zero-action state that both one-action and two-action maps collapse on for sufficiently strong perturbation. The model problem introduced below offers a way to investigate these aspects.

The present analysis concerns the bottom-wall-driven

[a]Present address: Institut für Geometrie und Praktische Mathematik, RWTH Aachen, Templergraben 55, D-52056 Aachen, Germany.

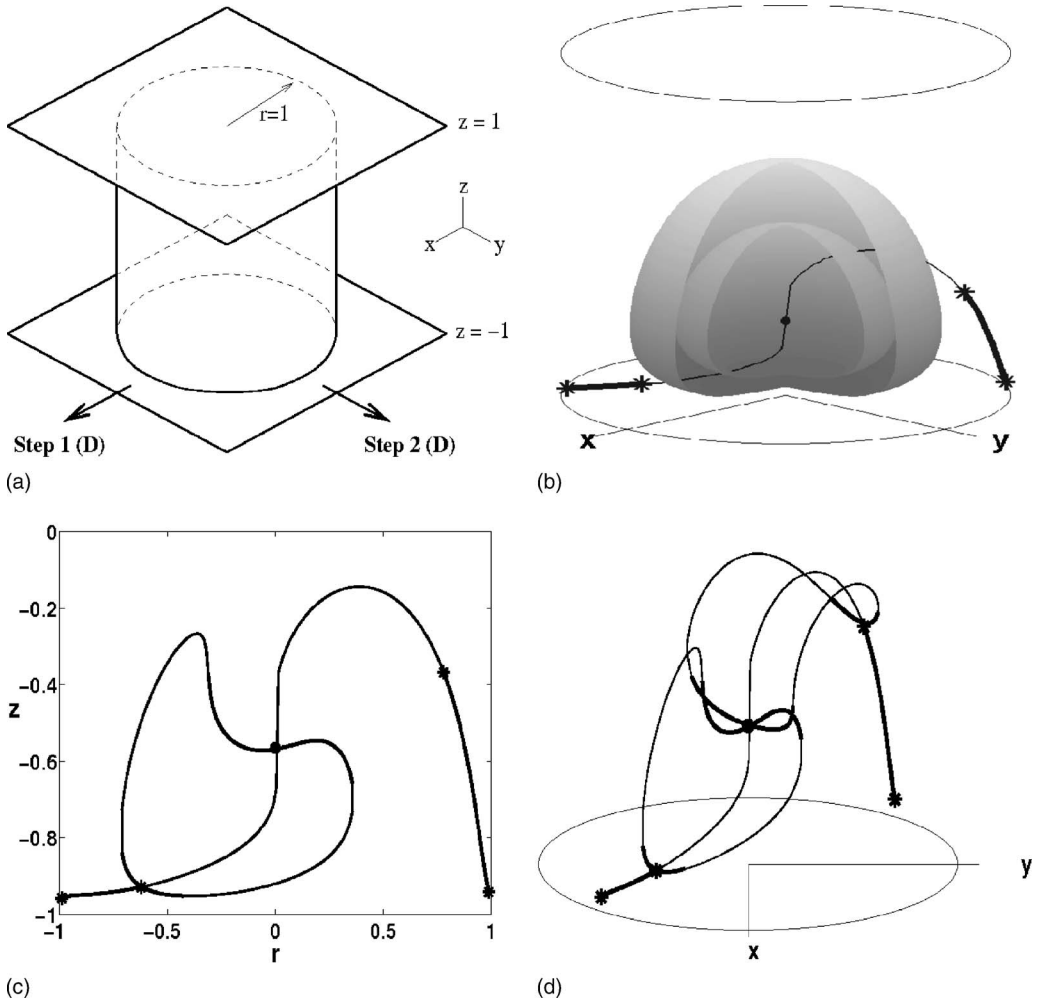

FIG. 1. Nondimensional model problem (a) and corresponding basic topological makeup in the noninertial limit Re=0 (b)–(d). (b) gives two invariant surfaces of the constant of motion F and the period-1 line in the plane $y=-x$; (c) and (d) give period-1 and period-2 lines in $y=-x$ and in 3D, respectively. Solid and heavy sections on the periodic lines are hyperbolic and elliptic segments, respectively; the dot is the parabolic stagnation point; the stars are the parabolic period-1 points.

time-periodic flow in a finite cylinder ("forcing protocol A") introduced in Speetjens *et al.*[16] In the noninertial Stokes limit (vanishing Reynolds number Re), this flow possesses one constant of motion with axisymmetric invariant surfaces topologically equivalent to spheres. Thus the model problem corresponds to a one-action map with invariant surfaces other than tori. The route from its one-action (inefficient mixing) to its zero-action (efficient mixing) state is explored in terms of the changes brought on to the noninertial topology with increasing perturbation by inertial effects due to nonzero Re.

The paper is organized as follows. Section II provides the problem definition and the employed numerical methods. The topology of the noninertial baseline flow is given in Sec. III. The topological changes brought on by inertial effects and the ramifications for the transport properties are discussed in Sec. IV. Conclusions are in Sec. V.

II. MODEL PROBLEM

An incompressible time-periodic flow $\boldsymbol{v}(\boldsymbol{x},t)$ is set up in the nondimensional square cylinder $\mathcal{D}:[r,\theta,z]=[0,1]\times[0,2\pi]\times[-1,1]$ by a two-step forcing protocol. The first and second forcing steps involve steady translation of the bottom wall in positive x and y direction, respectively, with fixed nondimensional displacement[17] $D=VT_f/2L=5$ (V, T_f, and L are respectively translation velocity, period time, and side length of the corresponding dimensional problem), and result under the present highly viscous conditions in stepwise steady flow. (Essentially unsteady effects involved with changeover between forcing steps are negligible under viscous flow conditions.) This forcing is repeated *ad infinitum* and thus generates a time-periodic flow. Figure 1(a) provides a schematic of the two-step time-periodic forcing protocol.

The motion of passive tracers is governed by the kinematic equation

$$\frac{d\boldsymbol{x}}{dt}=\boldsymbol{v}(\boldsymbol{x},t),\quad \boldsymbol{x}(0)=\boldsymbol{x}_0, \tag{1}$$

which describes the evolution of the positions $\boldsymbol{x}$ of tracers released at the position $\boldsymbol{x}_0$. The general solution to (1) reads $\boldsymbol{x}(t)=\boldsymbol{\Phi}_t(\boldsymbol{x}_0)$ and uniquely determines the current position $\boldsymbol{x}$

for a given initial tracer position $\boldsymbol{x}_0$. The corresponding volume-preserving map is defined by $\boldsymbol{x}_{k+1}=\boldsymbol{\Phi}_T(\boldsymbol{x}_k)$, with $\boldsymbol{x}_k$ the tracer position after k periods of the forcing protocol.

The flow $\boldsymbol{v}(\boldsymbol{x},t)$ on symmetry grounds admits an expression entirely in terms of the steady flow $\boldsymbol{u}(\boldsymbol{x})$ during the first step of each forcing cycle k:

$$\boldsymbol{v}(x,y,z,t)=\begin{cases}\boldsymbol{u}(x,y,z) & \text{for } (k-1)T\le t\le (k-1/2)T \quad \text{(first step)},\\ \boldsymbol{u}(y,-x,z) & \text{for } (k-1/2)T< t< kT \quad \text{(second step)},\end{cases} \tag{2}$$

advancing the steady flow $\boldsymbol{u}$ as the basic flow field.[16] This steady flow is governed by the nondimensional steady Navier-Stokes equations,

$$\mathrm{Re}\,\boldsymbol{u}\cdot\nabla\boldsymbol{u}=-\nabla p+\nabla^2\boldsymbol{u},\quad \nabla\cdot\boldsymbol{u}=0, \tag{3}$$

with p the pressure and $\boldsymbol{u}$ vanishing on all boundaries, except for the translation velocity U_x of the bottom wall in the x direction, which is specified below. The problem is characterized entirely by the Reynolds number $\mathrm{Re}=VL/\nu$, with ν the kinematic viscosity, which constitutes the single control parameter of the transport problem considered here.

Numerical resolution of the flow model (3) is performed by means of the spectral scheme proposed in Speetjens and Clercx.[18] This algorithm yields highly accurate solutions that admit satisfaction of the incompressibility constraint $\nabla\cdot\boldsymbol{u}=0$ up to near-machine precision. A performance analysis advanced very close approximation of this constraint as an essential prerequisite for reliable numerical studies on tracer advection in volume-preserving systems that conventional schemes tend to fall short of.[18] Numerical integration of the kinematic equation (1) employs an explicit third-order Taylor-Galerkin scheme and an interpolation scheme for the velocity field based upon its spectral expansion. Note the spectral scheme on numerical grounds imposes $U_x=(r^2-1)^2$ instead of the rigid-wall condition $U_x=1$ for the translation velocity U_x of the bottom wall. The changes in flow field brought on by this modification are entirely quantitative, however; topological properties are identical for both boundary conditions.[19]

III. THE NONINERTIAL BASELINE

The noninertial limit of $\boldsymbol{\Phi}_T$ [i.e., with the corresponding basic flow field $\boldsymbol{u}$ following (3) in the Stokes limit $\mathrm{Re}=0$] constitutes the baseline flow in terms of which to examine the effect of inertia upon the topology. This baseline flow is shown below to possess one constant of motion with axisymmetric invariant surfaces topologically equivalent to spheres. The underlying noninertial basic flow field $\boldsymbol{u}$ is of the form[20]

$$u_r(r,\theta,z)=\tilde{u}_r(r,z)\cos\theta,\quad u_\theta(r,\theta,z)=\tilde{u}_\theta(r,z)\sin\theta,$$
$$u_z(r,\theta,z)=\tilde{u}_z(r,z)\cos\theta, \tag{4}$$

with (r,θ,z) the cylindrical frame of reference. Its streamlines are closed and are self-symmetric about $x=0$ and form symmetric pairs about $y=0$. The closedness implies two constants of motion,[21] i.e., F_1 and F_2, which, consistent with (4), are of the form $F_{1,2}(\boldsymbol{x})=f_{1,2}(r,z)g_{1,2}(\theta)$. Substitution of the latter and (4) into the governing equation $\boldsymbol{u}\cdot\nabla F_{1,2}=0$ yields, via the method of separation of variables, $F_1(r,z)=f_1(r,z)$ and $F_2(r,\theta,z)=f_2(r,z)\sin\theta$ as corresponding general solutions. The axisymmetric constant of motion F_1 is retained by the time-periodic flow $\boldsymbol{v}$ according to (2); the constant of motion F_2 evidently is not. Hence, in the present context only F_1 is of relevance and, for brevity, denoted by F hereafter. Its governing equation is

$$\tilde{u}_r\frac{\partial F}{\partial r}+\tilde{u}_z\frac{\partial F}{\partial z}=0, \tag{5}$$

implying that within the (r,z) plane the isopleths of $F(r,z)$ coincide with the streamlines of the flow field $(\tilde{u}_r,\tilde{u}_z)$, which consist of concentric closed orbits centered upon a stagnation point on the cylinder axis. Thus the associated surfaces of revolution, defining the invariant surfaces of F in the 3D domain, comprise concentric and axisymmetric surfaces that are topologically equivalent to spheres.

The above exposed the noninertial limit of $\boldsymbol{\Phi}_T$ as a one-action map with invariant surfaces other than tori. Further topological features relevant in the current context are a period-1 line in the plane $y=-x$ and two period-2 lines, one within and one symmetric about this plane.[16,20] The basic topological makeup of the baseline flow is given in Figs. 1(b)–1(d). Figure 1(b) shows two of the concentric invariant surfaces of F and the period-1 line in the plane $y=-x$ (curve); Fig. 1(c) gives the period-1 line together with the period-2 line in $y=-x$; Fig. 1(d) shows the period-1 line and the two period-2 lines in perspective view. The solid and heavy sections on the periodic lines indicate hyperbolic and elliptic segments, respectively; the dot indicates the parabolic stagnation point on the hyperbolic segment upon which the invariant surfaces are centered; the stars are the parabolic period-1 points that bound the elliptic segments.[22] (Note the outer parabolic points coincide with the bounding wall.) The period-1 and period-2 lines intersect at the stagnation point and the two inner parabolic points on the period-1 line. Relevant topological features not shown for the sake of clarity are the manifolds associated with the hyperbolic segments of the periodic lines.[23]

The aforementioned symmetries in the streamline portrait of the basic flow $\boldsymbol{u}$ result in symmetries in the baseline flow.[16] These are given by

$$\mathbf{\Phi}_T^p = S_1 \mathbf{\Phi}_T^{-p} S_1, \quad p = 1,2,\ldots, \quad \mathbf{\Phi}_T = S_2 \mathbf{\Phi}_T S_2, \quad S_2 = S_3 \mathbf{\Phi}_{T/2}, \tag{6}$$

with $S_1:(x,y,z)\rightarrow(-y,-x,z)$ and $S_3:(x,y,z)\rightarrow(y,x,z)$ reflectional symmetries about the planes $y=-x$ ($\mathcal{S}$) and $y=x$, respectively, and $\mathbf{\Phi}_{T/2}$ is the map associated with the first forcing step. Symmetries reflect a degree of order in the flow and play an essential role in its topological makeup: S_1 is a time-reversal reflectional symmetry that first dictates coherent structures be symmetric about $\mathcal{S}$ and, second, implies the periodic lines in $\mathcal{S}$;[24] S_2 is an ordinary symmetry that imposes further topological restrictions on coherent structures. Moreover, symmetries are intimately related to the existence of constants of motion.[25] The response of the one-action map and its invariant surfaces to inertial perturbations thus is inextricably linked to the fate of the symmetries.

Tracers are in the noninertial limit restricted to invariant surfaces of F; within these invariant surfaces, motion is determined by the corresponding intrasurface topologies. These intrasurface topologies are shaped essentially by the periodic points defined by the intersection of the invariant surface with the period-1 and period-2 lines. The spatial variation in properties of the periodic lines (i.e., elliptic and hyperbolic segments) suggests multiple kinds of intrasurface topologies. Figure 2 gives several representative cases, with r_s the horizontal distance between the surface and the parabolic stagnation point (cross) upon which the invariant surfaces are centered. Figures 2(a)–2(d) show the invariant surfaces that intersect with the hyperbolic segment of the period-1 line and expose a topology that consists of two pairs of period-2 islands arranged around the two hyperbolic period-1 points (dots) and enveloped by their heteroclinically interacting manifolds (not shown). These two pairs of period-2 islands correspond with two pairs of period-2 elliptic points (facing points make one pair) that are on elliptic segments of the period-2 lines intersecting the invariant surface. [Here the elliptic segments that intersect at the stagnation point on the period-1 line are concerned; see Figs. 1(c) and 1(d). The influence of the other two elliptic segments on the period-2 lines is highly localized and thus left out of consideration.]

The periodic points belonging to periodic lines implies the map $\mathbf{\Phi}_T$ is locally area-preserving in their proximity.[15] (Important to note is that volume-preservation by the map $\mathbf{\Phi}_T$ does not entail local area preservation within invariant surfaces; the map preserves only the total area of an invariant surface.) This has the important implication that the periodic points and, consequently, the associated islands and manifolds, have properties that are essentially the same as found in area-preserving maps. This, in turn, means that, though the map is typically non-area-preserving away from the periodic points, the intrasurface dynamics are essentially similar to that of a Hamiltonian system. Hence the characteristic Hamiltonian intrasurface topologies (Fig. 2) that comprise coexisting KAM tori, island chains, and chaotic regions.

The progressive diminution of the period-2 islands and the formation of larger encircling islands and expanding chaotic regions with increasing r_s is phenomenologically similar to the progressive departure of a generic two-dimensional (2D) Hamiltonian systems from its integrable state by increasing the governing control parameter. Here r_s acts as control parameter for the state of the intrasurface topology. Figure 2(e) shows an invariant surface near the outermost (hyperbolic) segment of the period-2 lines and the parabolic point that connects the hyperbolic and elliptic segments of the period-1 line. The period-2 islands have vanished completely in favor of an entirely chaotic intrasurface state. Figure 2(f) shows an invariant surface that intersects with the outer elliptic segments of the period-1 line; intersections with the period-2 lines no longer occur. Here the topology consists of period-1 islands, associated with the elliptic segment of the period-1 line, embedded in an otherwise chaotic environment. Thus three kinds of intrasurface topologies can be distinguished. First, the period-2 islands on the inner invariant surfaces ["inner topology"; Figs. 2(a)–2(d)]; second, the period-1 islands embedded in a chaotic sea on the outer invariant surfaces ["outer topology"; Fig. 2(f)]; third, an intermediate set of invariant surfaces accommodating globally chaotic motion that separates the first and second regions ["intermediate topology"; Fig. 2(e)].

IV. INERTIAL FLOWS

A. General effects of inertia

Inertia introduces centrifugal forces to the circulatory basic flow $\boldsymbol{u}$ (i.e., the flow corresponding with the first forcing step; see Sec. II) that destroy its time-reversal reflectional symmetry about the plane $x=0$ of the noninertial limit.[16] This, in turn, destroys the time-reversal reflectional symmetry S_1 of the map $\mathbf{\Phi}_T$; only the ordinary nonreflectional symmetry S_2 is preserved for $\mathrm{Re}>0$. This symmetry breaking is the key that enables transition from the essentially 2D (one-action) state of the noninertial limit into the sought-after 3D (zero-action) state. Destruction of S_1 has two fundamental topological implications: (i) the constant of motion F vanishes and tracers are no longer restricted to invariant surfaces; (ii) the flow must no longer have periodic lines. The manifestation of these topological changes is elaborated below.

The centrifugal forces set up a secondary motion transverse to the primary motion within the invariant surface and cause drifting of tracers transverse to this invariant surface. This enables tracers to escape from the invariant surfaces and thus strictly results, consistent with the symmetry breaking, in vanishing of the constant of motion F for any $\mathrm{Re}>0$. The drifting tracers occupy a shell of finite thickness that is centered upon the invariant surface of the noninertial limit and gradually expands as time progresses. This behavior is demonstrated in Fig. 3 by means of the Poincaré section of a single tracer, shown in perspective view (top) and projected into the rz plane (bottom), for 10 000 forcing periods and several Re. Figure 3(a) gives the noninertial case ($\mathrm{Re}=0$) and clearly exposes the confinement of tracers to one invariant surface, implying essentially 2D (chaotic) advection. Figures 3(b) and 3(c) give the cases $\mathrm{Re}=0.1$ and $\mathrm{Re}=1$, respectively, and reveal the shell grows thicker with higher departures from the noninertial baseline. This implies the secondary

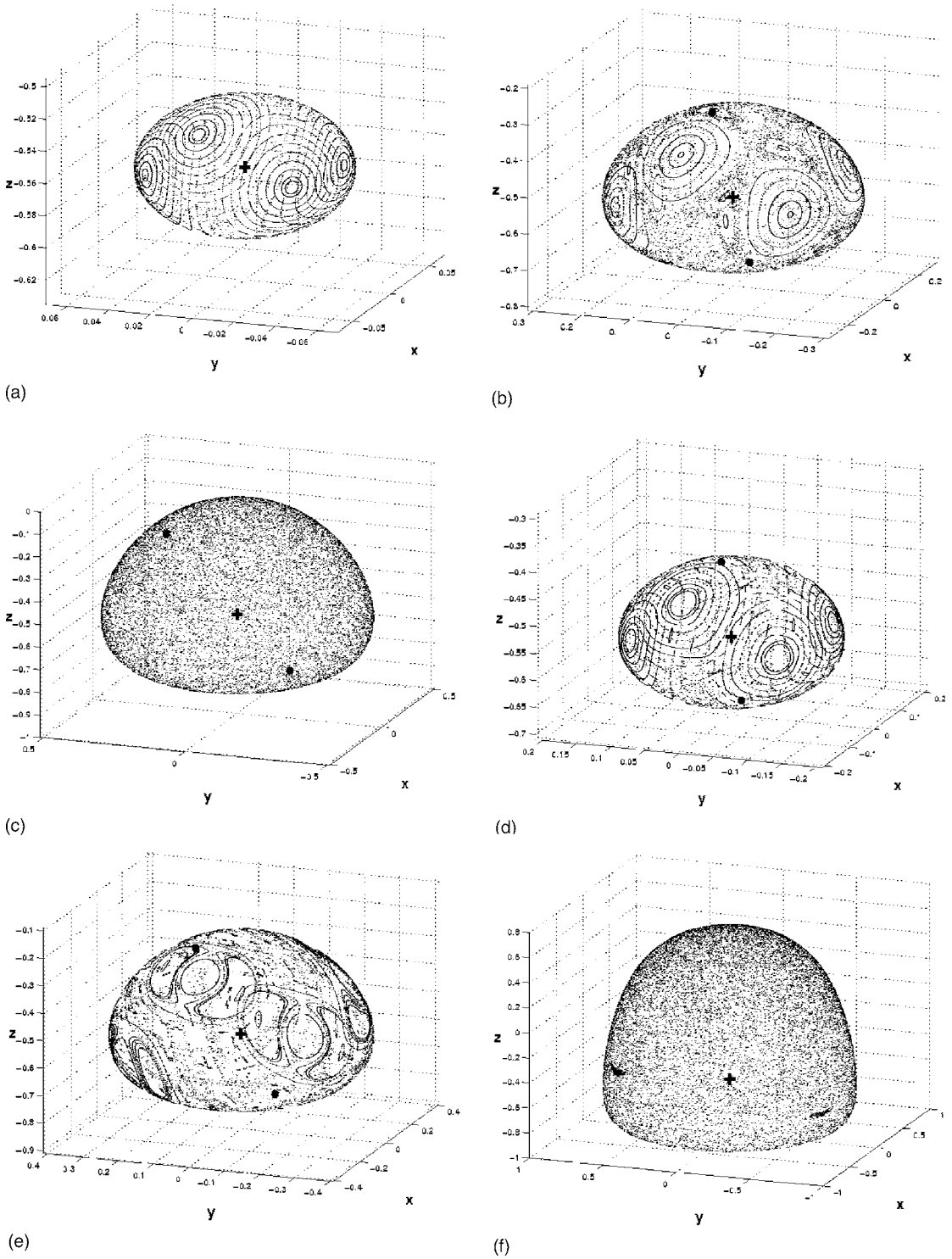

FIG. 2. Representative intrasurface topologies within the invariant surfaces in the noninertial limit; r_s is the horizontal distance between the invariant surface and the common center (cross). The dots in (a)–(e) indicate the two intersections of the invariant surfaces with the hyperbolic segment of the period-1 line; the left and right patches near the bottom in (f) are the elliptic islands centered upon the period-1 line. (a) $r_s=0.05$; (b) $r_s=0.15$; (c) $r_s=0.25$; (d) $r_s=0.35$; (e) $r_s=0.45$; (f) $r_s=0.8$.

motion gains in strength and consequently amplifies expansion rates of the shells with increasing Re. A measure for the expansion may be found in the fractal dimension D_f of the projected Poincaré section.[26] The lower and upper bounds correspond with the noninertial ($D_f=1$) and globally chaotic ($D_f=2$) cases, respectively; values $1<D_f<2$ reflect shells of finite thickness. Figure 4(a) shows the fractal dimension D_f after 10 000 forcing periods as a function of Re and reveals the system switches from a state of negligible expansion ($D_f\approx 1$) to a state of significant expansion ($D_f>1$) through a relatively narrow transient regime around $\mathrm{Re}\sim\mathcal{O}(1)$. Note the upper bound $D_f=2$ is never reached due to stagnation of fluid motion—preventing invasion of tracers—in the top-rim region of the cylinder.

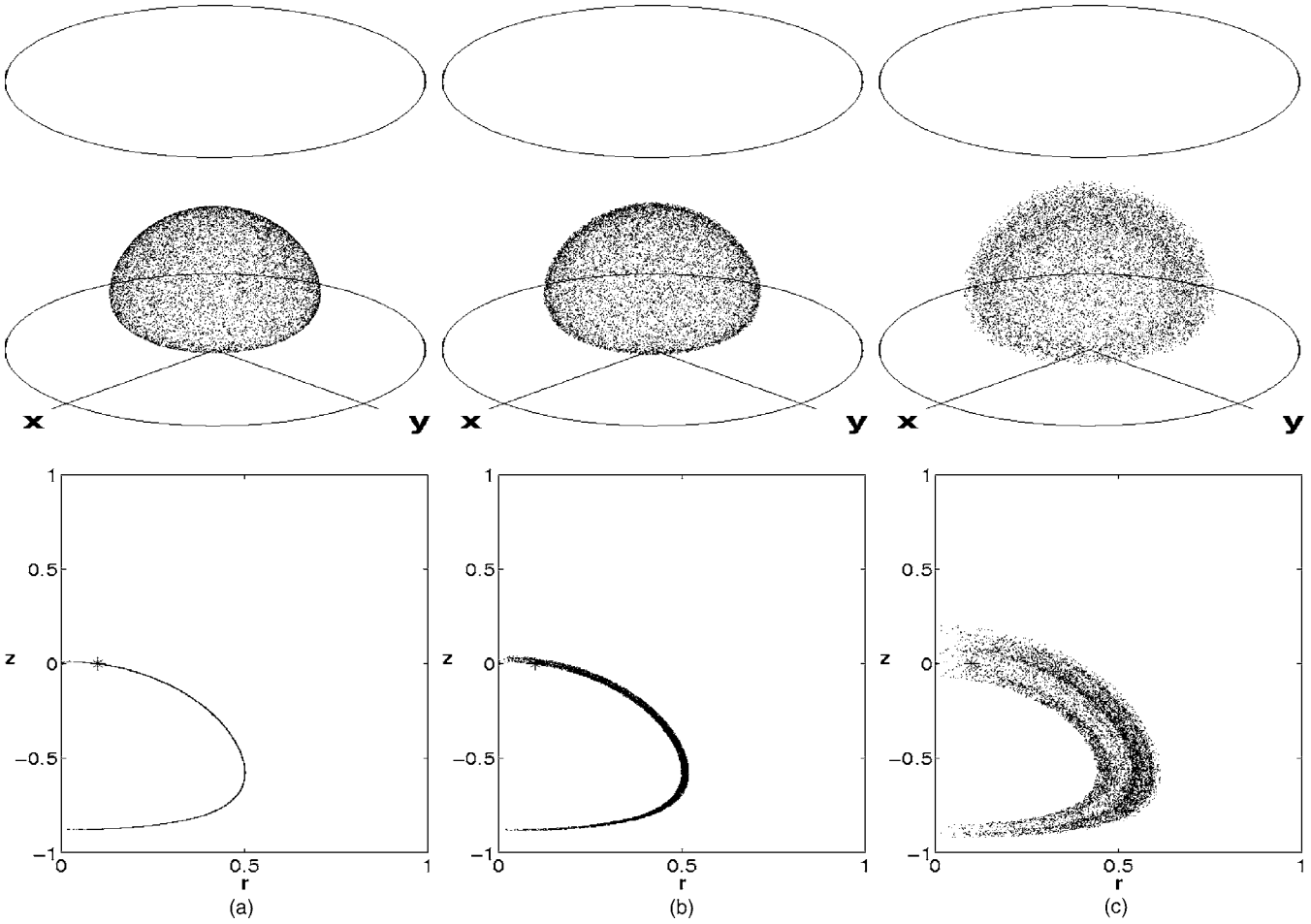

FIG. 3. Inertia-induced drifting of tracers transverse to invariant surfaces. Shown is the Poincaré section of a single tracer (10 000 periods) with increasing Re. The star represents the initial position $\boldsymbol{x}_0$ of the tracer. (a) Re=0; (b) Re=0.1; (c) Re=1.

The centrifugal forces destroy the periodic lines of the noninertial limit. The period-1 line transforms into an isolated period-1 point of the focus-type[22] (due to the circulatory motion of the fluid) and the one-dimensional (1D) unstable manifold of the accompanying manifold-pair for any $\mathrm{Re}>0$, thus implying the periodic-line state is a singular state.[27] The period-2 lines meet a similar fate. Measures for quantifying the effect of inertia may be found in the shortest horizontal distance δ from isolated period-1 point to $\mathcal{S}$ (degree of asymmetry) and the typical stretching rate λ effected by the manifolds of the period-1 point. [The latter follows from the eigenvalue spectrum

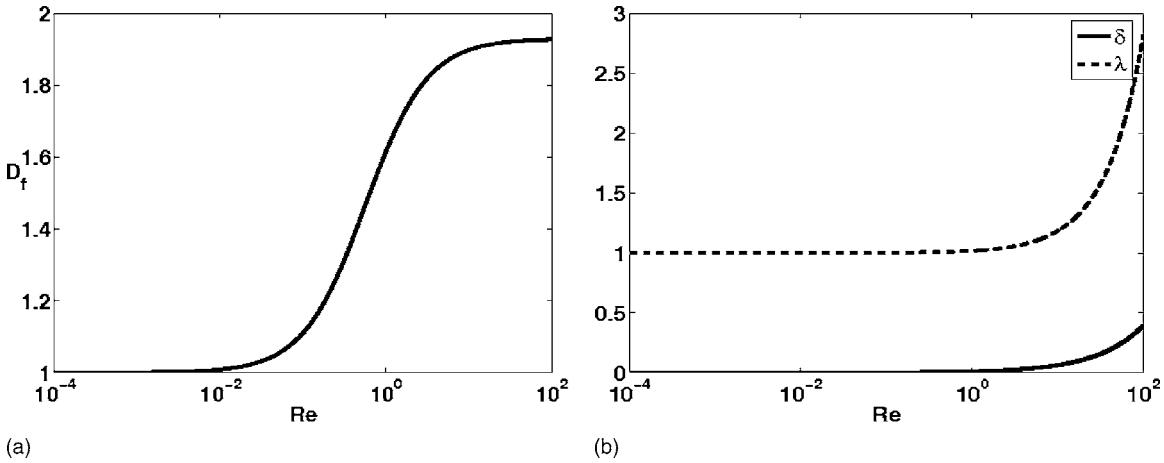

FIG. 4. General effect of inertia upon the topology quantified in terms of the fractal dimension D_f of the projected Poincaré section of a single tracer [(a); 10 000 periods] and the asymmetry δ and stretching rate λ of the period-1 point (b).

$\boldsymbol{\lambda}=(\lambda,\exp(i\phi)/\sqrt{\lambda},\exp(-i\phi)/\sqrt{\lambda})$ of the deformation tensor of the period-1 point,[22] with ϕ the local rate of fluid rotation.] Figure 4(b) gives δ and λ as a function of Re and reveals appreciable departures from the noninertial limit ($\delta=0$ and $\lambda=1$) require Reynolds numbers in excess of Re $\sim\mathcal{O}(1)$.

The above topological changes strictly set in for any $\mathrm{Re}>0$. However, Fig. 4 reveals up to $\mathrm{Re}\sim\mathcal{O}(1)$, the topology remains dominated by the invariant surfaces and the periodic lines; beyond $\mathrm{Re}\sim\mathcal{O}(1)$, the latter rapidly dissipate and the topology becomes dominated by the isolated period-1 point and its manifolds.[28] This suggests the transition from the one-action to the zero-action state involves essentially two topological states that successively occur for "small" ($\mathrm{Re}\lesssim\mathcal{O}(1)$) and "large" ($\mathrm{Re}\gtrsim\mathcal{O}(1)$) departures from the noninertial limit. These two topological states are elaborated in the following.

B. Small departures from the noninertial limit: Outer region

For small departures from the noninertial limit, significant transverse drifting of tracers involves time scales several orders of magnitude larger than the period time of the flow, meaning tracers remain entrapped in thin shells such as that shown in Fig. 3(b) for prolonged periods of time. This follows from the averaging principle.[29] Introduce to this end the action-angle coordinates $\boldsymbol{x}=(I,\phi,\varphi)$, with I the coordinate normal to the invariant surface (action), implying $F=F(I)$, and (ϕ,φ) the intrasurface coordinates (angles). This defines a natural frame of reference with the common center of the invariant surfaces as the origin ($I=0$) and I increasing monotonically with increasing distance from this center; the angles encompass the ranges $0\leq\phi\leq2\pi$ and $0\leq\varphi\leq\pi$. The map $\boldsymbol{x}_{k+1}=\boldsymbol{\Phi}_T(\boldsymbol{x}_k)$ is in the noninertial limit given by

$$I_{k+1}=I_k=I,\quad \phi_{k+1}=\phi_k+\omega_\phi(\boldsymbol{x}_k),\quad \varphi_{k+1}=\varphi_k+\omega_\varphi(\boldsymbol{x}_k), \tag{7}$$

with $\omega_{\phi,\varphi}$ the angular displacements within the invariant surface corresponding with $F(I)$ during one cycle. [The action remaining constant in (7) clearly reflects the confinement of tracers to said invariant surface.] For small departures from the noninertial limit, the map (7) becomes

$$I_{k+1}=I_k+\Delta I(\boldsymbol{x}_k),\quad \phi_{k+1}=\phi_k+\omega'_\phi(\boldsymbol{x}_k),\quad \varphi_{k+1}=\varphi_k+\omega'_\varphi(\boldsymbol{x}_k), \tag{8}$$

with $\Delta I\ll I_k$ the minute displacement transverse to the invariant surface induced by inertia and primes indicating small perturbation of the noninertial limit. Volume preservation dictates the average transverse displacement on invariant surfaces during one cycle be zero, implying $\int\int\Delta I(I,\phi,\varphi)s(I,\phi,\varphi)d\phi d\varphi=0$, with s a scaling factor due to the curvilinear action-angle coordinate system. This causes tracers to experience both inward ($\Delta I<0$) and outward ($\Delta I>0$) transverse displacements during their excursion in (predominantly) angular direction and consequently results in a quasioscillatory motion, i.e., $I_{k+1}\approx I+\Delta I(I,\phi_k,\varphi_k)$, around the unperturbed invariant surface corresponding with $F(I)$ within a thin shell of thickness $\mathcal{O}(|\Delta I|)$. (Note that for this principle to hold true it is essential that tracers sample substantial regions of this shell.) The confinement of tracers to the proximity of the unperturbed invariant surface implies the averaged map

$$I_{k+1}=I_k=\bar{I},\quad \phi_{k+1}=\phi_k+\omega'_\phi(\boldsymbol{x}_k),\quad \varphi_{k+1}=\varphi_k+\omega'_\varphi(\boldsymbol{x}_k), \tag{9}$$

with $\bar{I}=\mathcal{A}^{-1}\int\int(I+\Delta I(I,\phi,\varphi))s(I,\phi,\varphi)d\phi d\varphi=I$ and $\mathcal{A}=\int\int s(I,\phi,\varphi)d\phi d\varphi$, provides a good approximation to the perturbed map (8). Thus $F(\bar{I})$ acts as approximate constant of motion ("adiabatic invariant") under weakly inertial conditions.[29] The notion of adiabatic invariance is somewhat loose in the sense that tracers are not strictly confined to invariant surfaces of F, but are allowed limited freedom of movement in their direct proximity.[30] Here $\bar{I}=I$ and this freedom causes the formation of thin shells ("adiabatic shells") centered upon the invariant surfaces of the noninertial limit [Fig. 3(b)].

Further families of adiabatic structures emanate from the period-2 and period-1 islands in the inner and outer topologies, respectively, of the invariant surfaces (see Sec. III). These islands consist of closed orbits that encircle periodic lines and coincide with a given invariant surface of F. This has the important consequence that, in the local intrasurface frame of reference (ϕ,φ), the map $\boldsymbol{\Phi}$ is area preserving,[15] meaning the closed orbits identify with level curves of a local Hamiltonian $H(\phi,\varphi)$. Thus the tracer dynamics are locally governed by two constants of motion, namely, $F(r,z)$ and $H(\phi,\varphi)$, implying $\boldsymbol{\Phi}$ is locally a two-action map. Perturbation of such a map effectuates coalescence of the closed orbits into tubes parametrized by an adiabatic invariant[6] and transforms the local two-action map into a local one-action map.[31] This coalescence follows from essentially the same averaging principle as outlined above, albeit here applying locally in the zone occupied by the islands. Thus families of concentric tubes, centered upon elliptic segments of the periodic lines, are created. The perturbed map $\boldsymbol{\Phi}$ thus accommodates multiple families of coherent structures, viz., the adiabatic shells corresponding with F and the families of concentric tubes corresponding with the elliptic segments of the periodic lines. However, these families, rather than coexist, appear to interact. Such interaction and its effect upon the tracer dynamics is elaborated below.

In the outer-topology region, two adiabatic shells of F connect via one tube on each elliptic segment of the period-1 line and form one adiabatic structure. Figure 5 shows such a structure in perspective view [Fig. 5(a)] and its portion in a thin slice centered upon $\mathcal{S}$ [Fig. 5(b)], together with the period-1 line (curve) for $\mathrm{Re}=0.1$. The merger occurs such that fully closed adiabatic structures are formed that enclose one another. This arrangement is demonstrated in Fig. 6 for the structure of Fig. 5 and a second structure. Note the outer shell of the latter virtually coincides with the boundary. The family of adiabatic structures thus created is on the inside and outside bounded by the fully preserved adiabatic shells

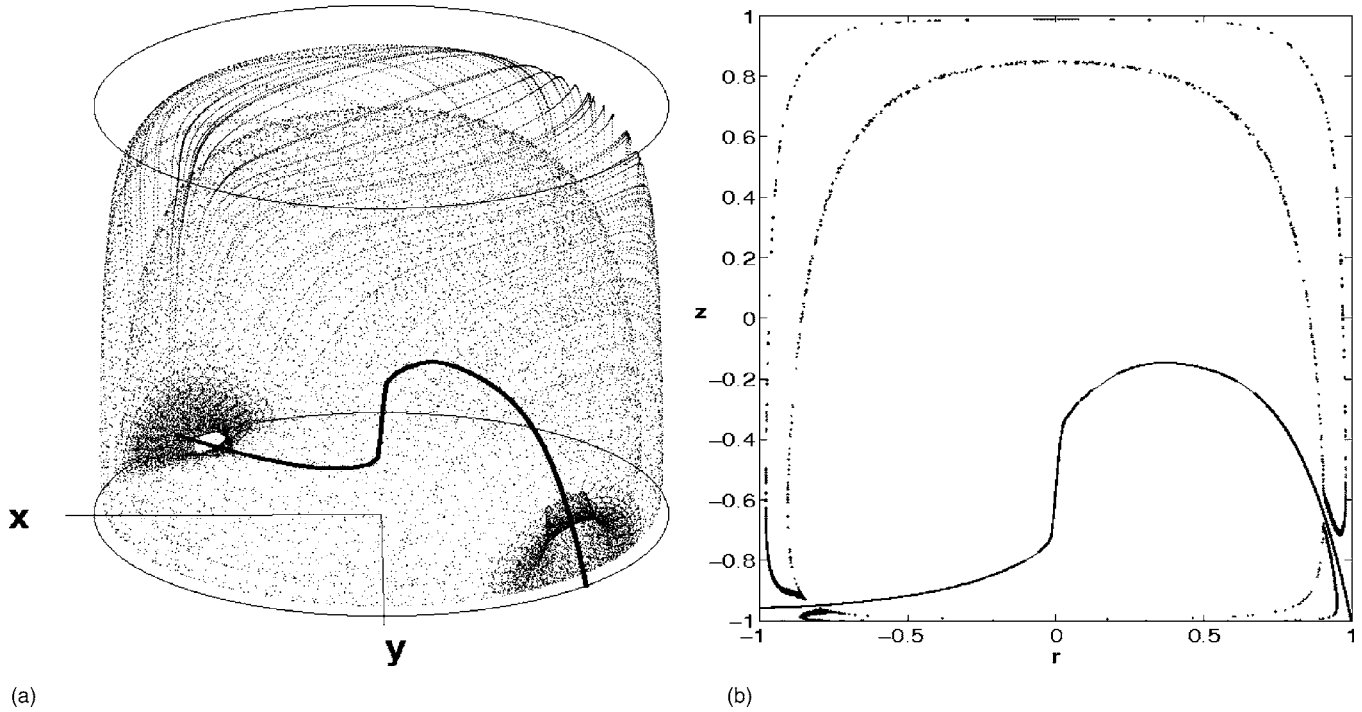

FIG. 5. Resonance-induced merger of adiabatic shells corresponding with F with elliptic tubes emanating from the elliptic segments of the period-1 line (curve) for small departures from the noninertial limit (Re=0.1). (a) Perspective view; (b) slice centered upon S.

of the intermediate topology and the domain boundary, respectively, and constitutes the adiabatic state of the outer-topology region.

The cause for the merger must be sought in the local breakdown of the averaging principle, which underlies the formation of adiabatic structures,[29] at the ends of the tubes. This breakdown leads to local "openings" in the adiabatic shells that enable switching of tracers between tubes and shells, thus effectively connecting them. Key to the formation of an adiabatic shell is that tracers sample substantial regions of the invariant surface so that the corresponding averaging principle underlying (9) is upheld. This essential condition is violated in the proximity of the parabolic periodic points that bound both ends of the elliptic segments of the period-1 line, where fluid parcels deform (shear) yet perform no (appreciable) net motion. Tracers released in posi-

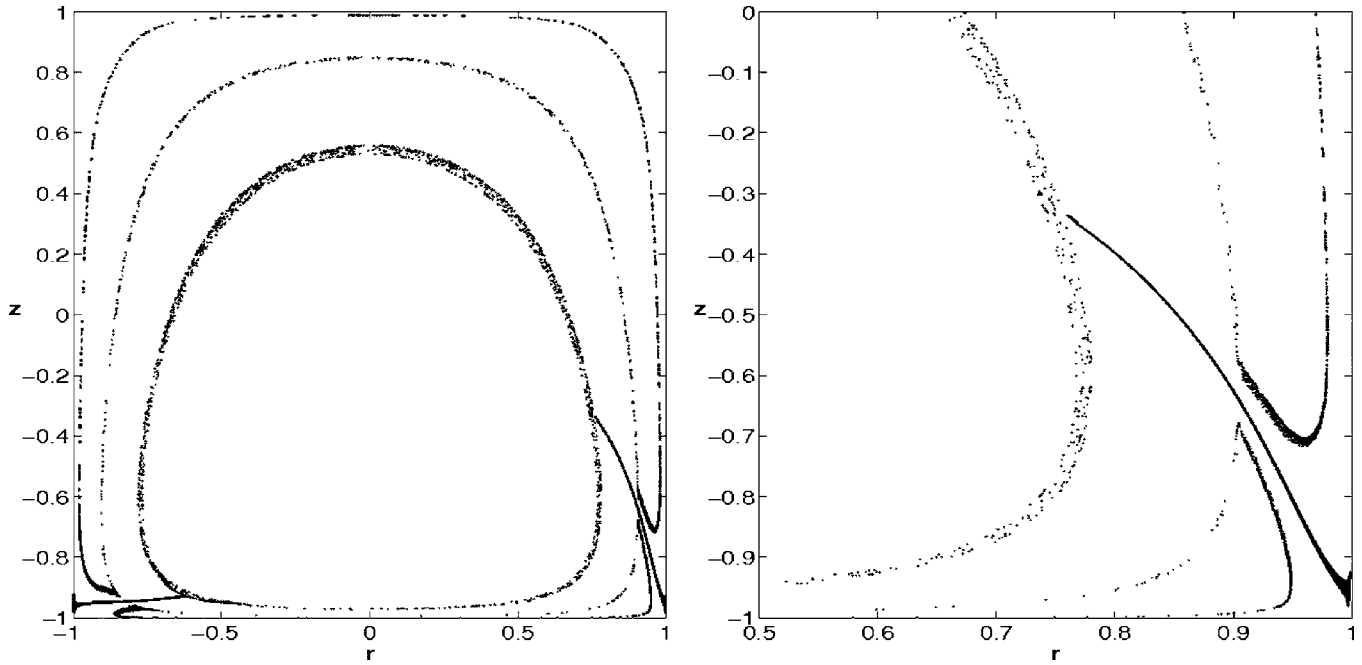

FIG. 6. Arrangement of adiabatic structures in the outer-topology region for small departures from the noninertial limit (Re=0.1). Shown are the slices centered upon S.

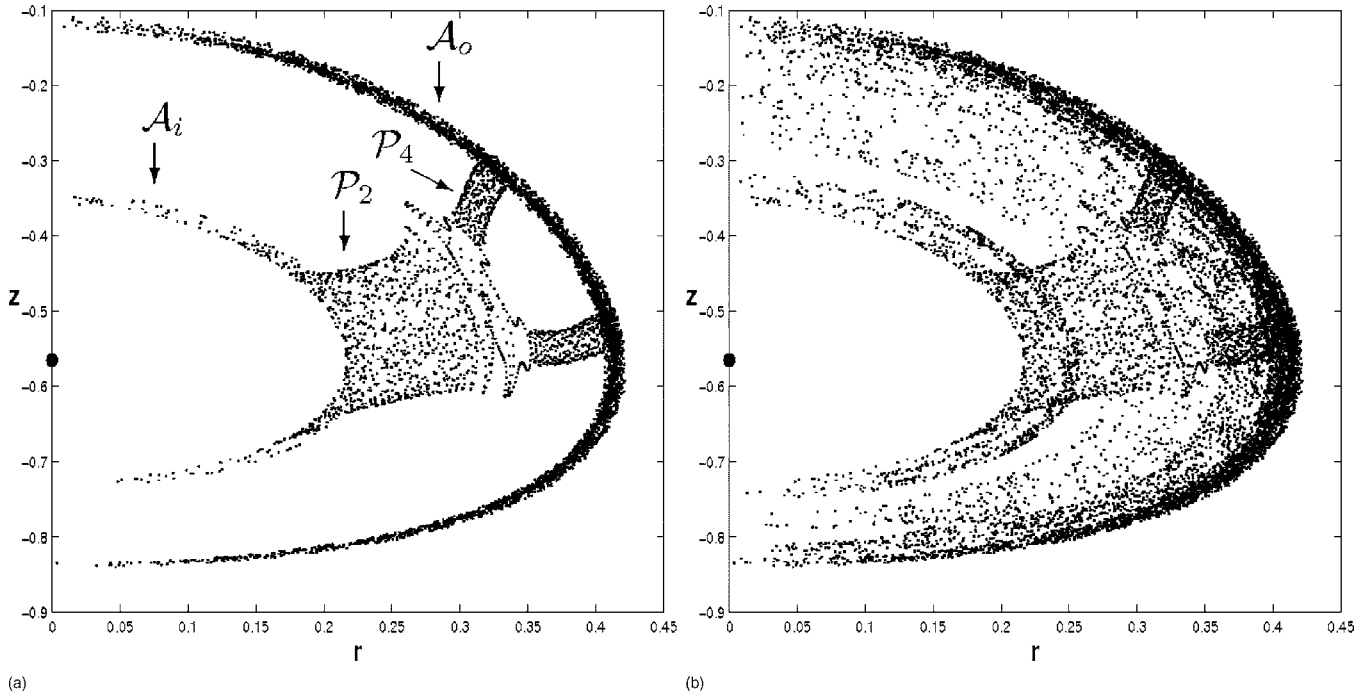

FIG. 7. Adiabatic behavior in the inner-topology region for small departures from the noninertial limit (Re=0.1). (a) demonstrates the connection of the inner ($\mathcal{A}_i$) and outer ($\mathcal{A}_o$) shell through the linked period-2 ($\mathcal{P}_2$) and period-4 ($\mathcal{P}_4$) tubes that define adiabatic structures such as that shown. (b) shows the adiabatic structure embedded in the chaotic environment created through leakage of the shells. Shown are the projections in the rz plane.

tions $\boldsymbol{x}_0$ close to such periodic points systematically return to the same localized region and thus are subject to approximately the same transverse displacement, i.e., $I_{k+1} \approx I_0 + k\Delta I(I_0, \phi_0, \varphi_0)$, during (initial) forcing cycles and, consequently, start to resonate. This resonance causes tracers to progressively move away from the invariant surface rather than perform the quasioscillatory motion that is at the base of (9) and consequently results in local breakdown of the averaging principle.[6] Thus the adiabatic shells develop local defects, creating the abovementioned "openings" that facilitate the merger of adiabatic shells and tubes.[32] Moreover, this implies that chaotic motion in an invariant surface, which is inherently nonresonant, is imperative to its survival as an adiabatic shell.

Resonances are hitherto known only to cause (local) breakdown of coherent structures in one- and two-action maps (see Sec. I). However, for the one-action map studied here the resonances in the outer-topology region cause merger of structures. This is a fundamental difference that sets the behavior found here apart from that known to date and thus suggests an essentially new response scenario: resonance-induced merger.

C. Small departures from the noninertial limit: Inner region

In the inner-topology region, mechanisms similar to those found for the outer-topology region are at work. This basically results in a similar response to weakly inertial effects: coalescence of islands into tubes and resonance-induced merger (RIM) of tubes with adiabatic shells. Note here four connections between inner and outer shells are formed, each corresponding with one period-2 island of the noninertial limit. However, as opposed to the outer-topology region, strong variation in intrasurface topologies exists in that the period-2 islands significantly diminish via the continuous disintegration of the outer KAM tori into higher-order island chains with increasing distance r_s to the common center [see Figs. 2(a)–2(d)]. Furthermore, the islands and encircling island chains, in contrast with the strongly localized period-1 islands in the outer-topology region, occupy a significant part of the invariant surface. This has essential consequences for the adiabatic behavior. Figure 7(a) shows one of the four connections of a representative adiabatic structure in the inner-topology region (rz projection) for Re=0.1 that, akin to the outer-topology structures (Fig. 5), is composed of one inner ($\mathcal{A}_i$) and one outer ($\mathcal{A}_o$) adiabatic shell interconnected through tubes. However, two essential differences with the outer-topology structures occur. First, the adiabatic shells are, rather than via one continuous tube, connected through one period-2 tube ($\mathcal{P}_2$) linked with two period-4 tubes ($\mathcal{P}_4$). Second, the adiabatic shells are "leaky" and randomly exchange material with the environment. This leakage creates a chaotic environment that surrounds the adiabatic structures [see Fig. 7(b)] and enables tracers to randomly switch structures in a manner reminiscent of RID (see Sec. I). Furthermore, this leakage causes the four tube-shell connections to effectively become disconnected and form individual adiabatic structures that emerge in clusters of four.

The tube-shell connections result from RIM triggered by the parabolic stagnation point ($\mathcal{A}_i$) and the parabolic points bounding the outer end of the elliptic segments of the periodic lines associated with the period-4 tubes ($\mathcal{A}_o$). The linked period-2/period-4 tubes emanate from the transforma-

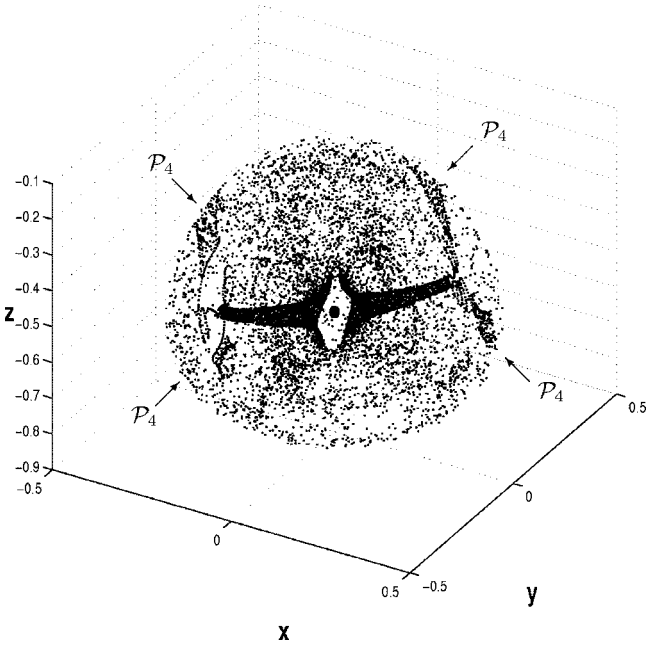

FIG. 8. 3D extent of adiabatic structures in the inner-topology region for small departures from the noninertial limit (Re=0.1). Shown are two structures that each correspond with one of two facing elliptic islands. Both structures are embedded in a chaotic cloud that results from material emitted by the leaky inner shells and is bounded by the leaky outer shell attached to the period-4 tubes ($\mathcal{P}_4$).

tion of coalescing adjacent orbits from KAM tori to island chains with increasing r_s through the Poincaré-Birkhoff mechanism[14] by which the period-2 tube effectively disintegrates into the two period-4 tubes at some r_s. [Note the period-4 tubes correspond with the period-4 islands encircling the remnant of the period-2 island in Fig. 2(d).] Transformation of an orbit from the KAM torus into an island chain takes place via an intermediate state termed cantorus.[33] Such cantori are in fact KAM tori that have developed gaps and are thus partitioned into disconnected segments, along which tracers perform quasiresonant motion as a precursor to the resonant motion that underlies the eventual breakup into an island chain. This quasiresonant motion causes local breakdown of the averaging principle and thus, given a whole set of cantori exists near the outer end of period-2 tubes, creates an intermediate chaotic region through which tracers switch randomly between the families of period-2 and period-4 tubes. Numerical analysis strongly suggests the intermediate region connects only the two families of tubes; tracers escaping from this region into its environs, though not ruled out conclusively, has not been observed. This, in turn, suggests an interplay of RIM (merger of both families induced by the parabolic points at the end of the tubes) and RID-like behavior (random switching between both families induced by cantori).

Cantori also underlie the leakage of the adiabatic shells. The island chains encircling the period-2 islands are invariably accompanied by cantori[33] that lead to "holes" in the adiabatic shells through which material "leaks" into the environment. The 3D extent of the adiabatic structures is demonstrated in Fig. 8 for two structures of one cluster of four, each corresponding with one of two facing elliptic islands, in perspective view. (Note for lucidity other structures than that in Fig. 7 are shown.) The period-2 tubes each extend away in opposite direction from disconnected remnants of the inner adiabatic shell and disintegrate into (barely discernible) period-4 tubes ($\mathcal{P}_4$) at some distance r_s from the stagnation point (dot). Both structures are embedded in a chaotic cloud that results from material emitted by the leaky shells and is bounded by the outer adiabatic shell attached to the period-4 tubes. The adiabatic structures studied above are the principal building blocks of the inner-topology region in the present regime. Other structures involving (interacting) higher-order tubes, though existence is probable, are believed of negligible influence upon the global transport properties within the inner-topology region and have on those grounds been left out of consideration.

The adiabatic topology disclosed above determines the tracer transport as follows. In the outer-topology region, both tubes transport material from the inner to the outer shell. The residence time of tracers in the tubes ($T_{\mathcal{P}}$) during this transport is typically $T_{\mathcal{P}}/T \sim \mathcal{O}(1000)$. Figure 9 demonstrates this migration from the inner ($\mathcal{A}_i$) to the outer ($\mathcal{A}_o$) shell through the period-1 tube ($\mathcal{P}_1$) in the second [Fig. 9(a)] and fourth [Fig. 9(b)] quadrant of the structure in Fig. 5 in terms of the evolution of r_s of the tracer released midway the tube that is utilized to visualize the structure. (n is the number of forcing periods undergone by this tracer.) Mass conservation suggests the typical residence time of tracers on the inner shell ($T_{\mathcal{P}}$) prior to extraction by one of the tubes scales as $T_{\mathcal{A}}/T_{\mathcal{P}} \sim (L_{\mathcal{A}}/L_{\mathcal{P}})^2$, with $L_{\mathcal{A}}$ and $L_{\mathcal{P}}$ the typical length scales of shell and tube, respectively.[34] Given $L_{\mathcal{A}}/L_{\mathcal{P}} \gg 1$, this implies residence times on the inner shell exceed those of the tubes by several orders of magnitude, meaning tracer extraction from the inner shells is an extremely slow process.[35] In the inner topology, tracers are through the outer "leaky" shell ($\mathcal{A}_o$) of an adiabatic structure extracted from the chaotic environment and via the two attached period-4 tubes ($\mathcal{P}_4$) inwardly transported toward the intermediate chaotic region that connects the period-2 and period-4 tubes, respectively. In this connecting region, tracers switch randomly between period-4 and period-2 tubes and migrate further inward through the period-2 tube ($\mathcal{P}_2$) to the "leaky" inner shell ($\mathcal{A}_i$) and are released into the chaotic environment again. This behavior is demonstrated in Fig. 10 for the adiabatic structure of Fig. 7 in terms of r_s. (Note the smooth switching from period-4 to period-2 tubes.) Tracers released in the inner-shell region gradually work their way outwards again through the chaotic environment until renewed extraction and inward transportation by an adiabatic structure occurs. This process is repeated *ad infinitum* and the adiabatic structures thus set up a circulation within the inner-topology region. Note residence times in structures are typically in the order of 1000 periods.

D. Large departures from the noninertial limit

For large departures from the noninertial limit, the adiabatic structures vanish and the topology becomes dominated by the isolated period-1 point of the focus-type and its asso-

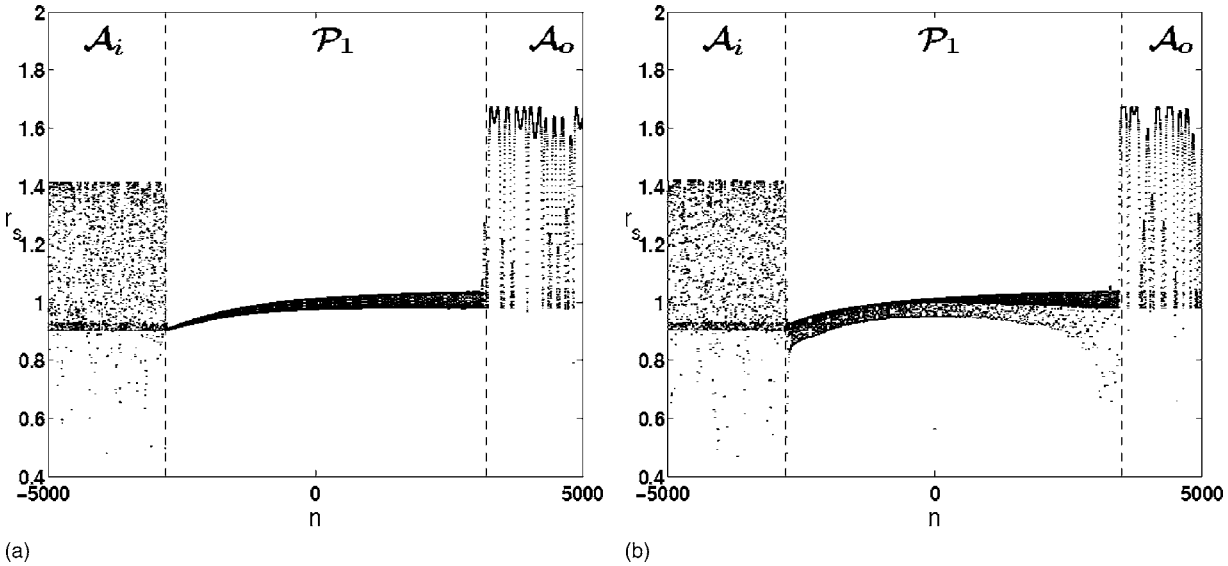

FIG. 9. Tracer transport through the period-1 tubes in the outer-topology region. Shown is the migration of the tracer released midway the tube that is utilized to visualize the structure from the inner ($\mathcal{A}_i$) to outer ($\mathcal{A}_o$) shell through the period-1 tube ($\mathcal{P}_1$) in the second (a) and fourth (b) quadrant of the structure in Fig. 5 in terms of the evolution of r_s. (n is the number of forcing periods undergone by this tracer; $n>0$ and $n<0$ correspond with forward and backward progression in time, respectively.)

ciated manifolds (see Sec. IV A). Figure 11 shows the 2D stable [Fig. 11(a)] and 1D unstable [Fig. 11(b)] manifolds associated with the period-1 point [the star in Fig. 11(b)] at Re=100. The intricate shape of both manifolds reflects the essentially 3D nature of the map $\mathbf{\Phi}$. In 3D time-periodic systems, the occurrence of periodic structures only as isolated points is a sufficient condition for global chaotic advection.[16] The map $\mathbf{\Phi}$ meets this condition and thus admits global chaotic tracer dynamics for sufficiently high Re. This is substantiated further by the fact that the manifolds exhibit transverse homoclinic interaction, as demonstrated in Fig. 12, that effectuates exponential stretching and folding of fluid parcels (one of the classical "fingerprints of chaos"[37]). The truly 3D nature of the tracer motion for large Re is demonstrated in Fig. 13, showing the Poincaré section of an individual tracer (10 000 periods) for Re=10 [Fig. 13(a)] and Re=100 [Fig. 13(b)] to cover the entire flow domain, consistent with the corresponding fractal dimension approaching the upper bound $D_f=2$ (see Fig. 4). (Note that the absence of tracer positions in the upper-right corner reflects the local stagnation of fluid motion that inhibits tracer invasion in the top-rim region and thus prevents D_f from reaching its upper bound.) This conclusively establishes the unrestricted freedom of motion that is the hallmark of globally chaotic advection.

The system thus smoothly transits from a one-action

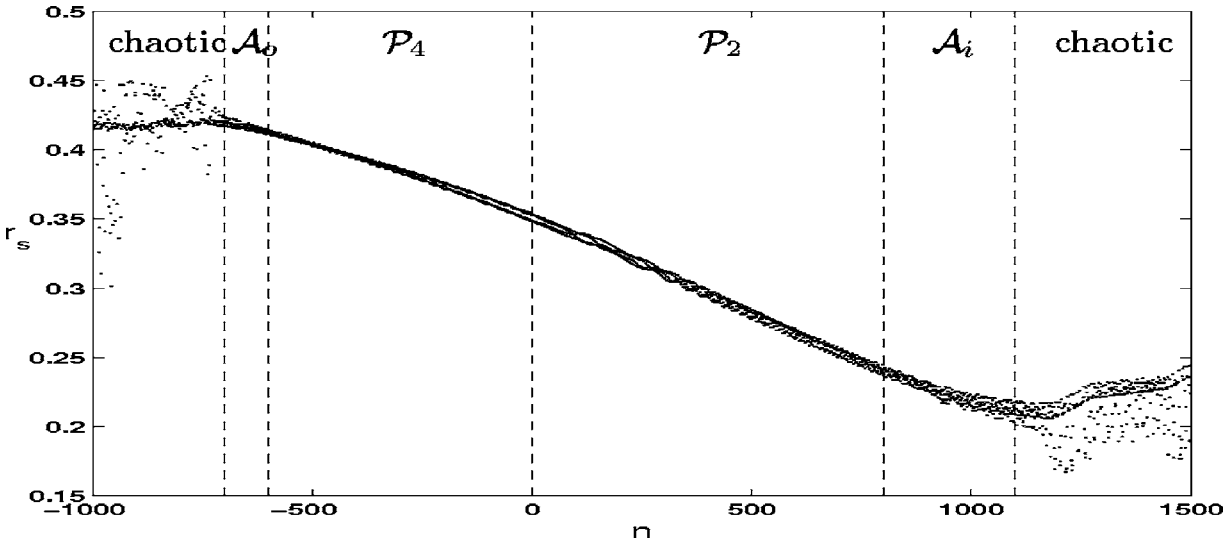

FIG. 10. Tracer transport through the adiabatic structures in the inner-topology region. Shown is the migration of a tracer extracted from the chaotic environment from the outer shell ($\mathcal{A}_o$) through the period-4 ($\mathcal{P}_4$) and period-2 ($\mathcal{P}_2$) tubes to the inner shell ($\mathcal{A}_i$) of the structure in Fig. 7 and the subsequent release into the chaotic environment in terms of the evolution of r_s. (n is the number of forcing periods; $n>0$ and $n<0$ correspond with forward and backward progression in time, respectively.)

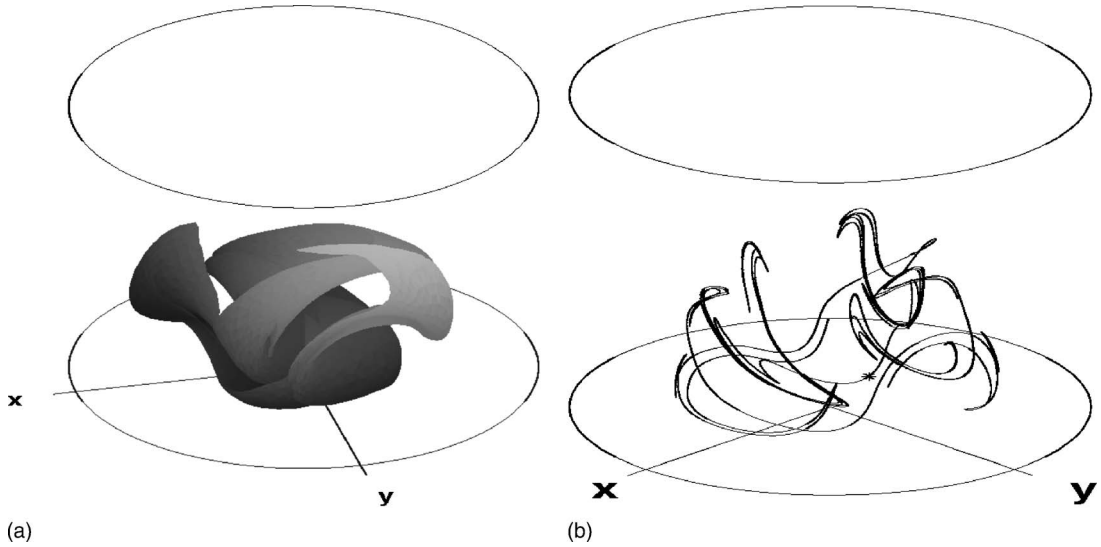

FIG. 11. Manifold pair corresponding with the isolated period-1 point for large departures from the noninertial limit. Shown are the stable 2D manifold (a) and the unstable 1D manifold (b) for Re=100.

state into a zero-action state with increasing inertia. The absence of constants of motion in the zero-action state implies absence of corresponding invariant surfaces and curves. However, coherent structures—and thus a topology—are present nonetheless. Brouwer's fixed-point theorem[38] predicts for convex flow domains (e.g., the present cylinder) at least one isolated period-1 point and, given the inherently hyperbolic nature of such points,[20] an associated manifold pair, implying the topology of zero-action maps in convex domains is essentially similar to that shown in Fig. 12. For nonconvex domains (e.g., interior of a torus) an equivalent theorem is missing and the topological makeup of the corresponding zero-action state is less clear. However, irrespective of topological properties of the flow domain, in general a topology composed of the basic building blocks, i.e., periodic lines and points and corresponding manifolds, is to be expected.

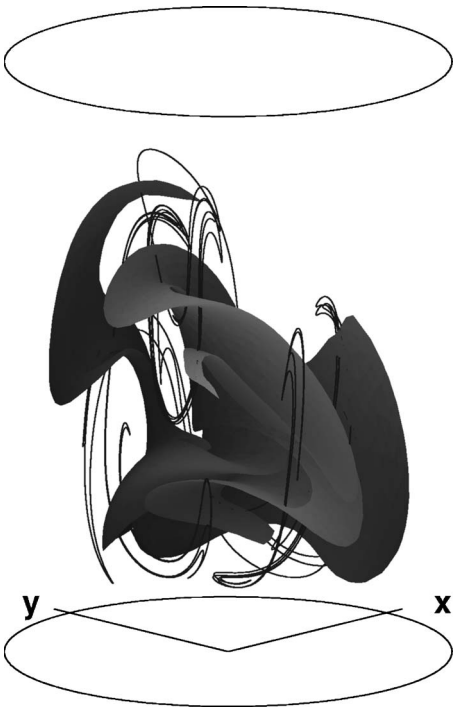

FIG. 12. Transverse homoclinic interaction by the stable 2D manifold (surface) and the 1D unstable manifold (curve) of the period-1 point for Re =100.

V. CONCLUSIONS

The work presented here is performed in the scope of viscous mixing flows and concerns a numerical analysis of the effect of inertia upon the topology and associated transport properties of an incompressible time-periodic flow in a finite cylinder. The properties of this time-periodic flow are examined in terms of volume-preserving maps. In the noninertial limit, the flow corresponds to a one-action map with invariant surfaces other than tori and thus belongs to a subclass of volume-preserving maps that is largely unexplored to date. The route from its one-action (inefficient mixing) to its zero-action (efficient mixing) state is analyzed in terms of the changes in the noninertial topology with increasing inertia (control parameter Re). The findings of this analysis are elaborated on below.

Inertial effects cause symmetry breaking and thus fundamentally alter the system. This symmetry breaking implies that, first, tracers are no longer restricted to invariant surfaces of the constant of motion F and, second, the flow must no longer accommodate periodic lines. This destroys the topological constraints of the noninertial one-action state and paves the way toward the zero-action state. Manifestations of inertia are expansion of the invariant surfaces into shells and transformation of the periodic lines into isolated periodic points. Transition from the one-action to the zero-action state with increasing Re involves essentially two topological states that correspond with "small" and "large" departures from the noninertial limit. The former state is dominated by the invariant surfaces and the periodic lines; the latter state is dominated by the isolated period-1 point and its manifolds.

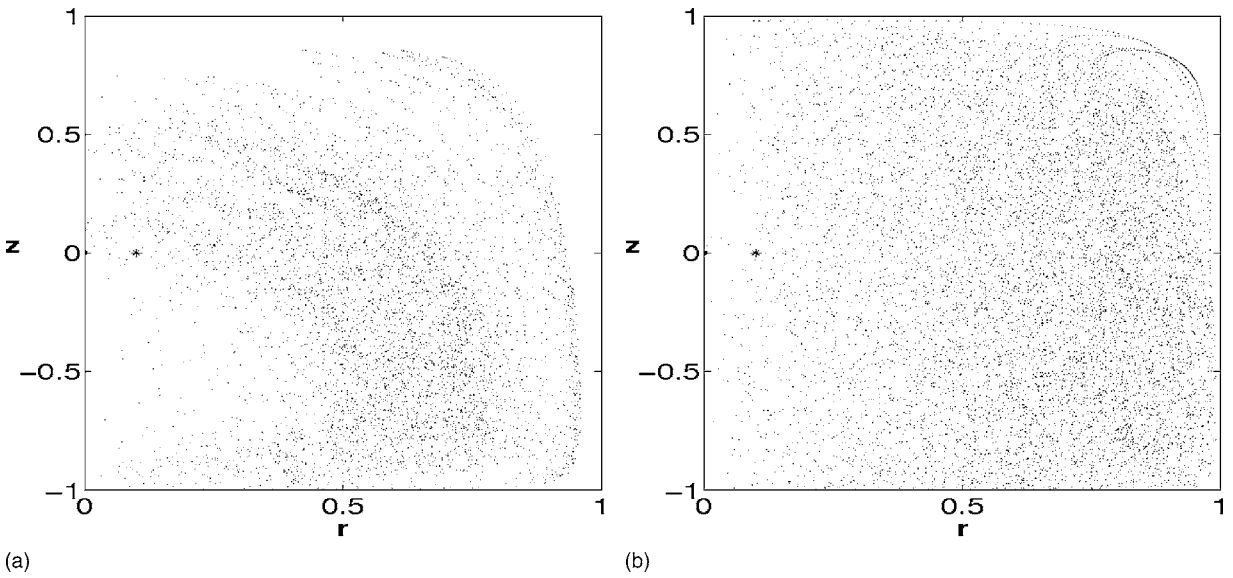

FIG. 13. 3D globally chaotic advection for large departures from the noninertial limit. Shown are the projections of the Poincaré sections of a single tracer (10 000 periods) in the rz plane for Re=10 (a) and Re=100 (b). The star indicates the initial position $\boldsymbol{x}_0$ of the tracer.

Small departures from the noninertial limit result in an adiabatic state in which invariant surfaces expand into thin shells and elliptic islands of periodic lines coalesce into tubes. These shells and tubes interact and form two families of adiabatic structures that each occupy an inner-topology and outer-topology region spatially separated by a family of noninteracting fully intact shells. The outer-topology structures consist of inner and outer shells interconnected through period-1 tubes and are fully closed. The inner-topology structures consist of "leaky" inner and outer shells interconnected through linked period-2/period-4 tubes. The leakage enables random in/outflux of material and creates a chaotic environment in the inner-topology region in which the adiabatic structures are embedded. The formation of chaotic regions in an otherwise one-action-like topology (dense sets of essentially 2D structures) is the first step toward the zero-action state.

Resonances are the key mechanism that facilitates the merger and (local) disintegration of structures and essentially shape the adiabatic topology described above. In the proximity of resonances (parabolic points and cantori of the noninertial limit) the adiabatic structures develop local defects due to breakdown of the averaging principle. Defects from parabolic points result in merger of tubes and shells through an essentially new response scenario: resonance-induced merger (RIM). Defects from cantori cause the leakage of shells and, upon interplaying with parabolic points, the linkage of the families of period-2 and period-4 tubes in the inner-topology region. Similar cantori-induced effects in the outer-topology region have not been observed and are believed either negligible or nonexistent at all due to the highly localized nature of the period-1 islands and the only little spatial variation in their topological properties.

Resonances inducing dispersion are well known (see Sec. I). Resonances inducing merger are not. Here dispersion and merger follow from cantori and isolated parabolic points, respectively, and may occur isolated (tube-shell merger and shell-leakage) or combined (period-2/period-4 linkage). A full understanding of the resonance-induced behavior found here is lacking. However, the following factors are believed important. The "strength" of resonances varying with its order[8] (cantori are approximately chains of higher-order parabolic points) may play a role in the fundamental difference in behavior caused by isolated (low-order) parabolic points and (high-order) cantori. Moreover, the topological equivalence of the invariant surfaces to spheres is presumed key for the RIM. First, this invalidates the Hamiltonian response scenarios for one-action maps, which hold only for tori, suggesting the dynamics are governed by fundamentally different scenarios. Second, this causes resonances to typically emerge as isolated points bounding elliptic segments on periodic lines rather than as separate curves (one-action maps with tori) or surfaces (two-action maps). Sphere-like invariant surfaces namely usually accommodate isolated periodic points that, through connectivity of fluid parcels, join with adjacent points into one (or more) periodic lines intersecting the invariant surfaces.[15] Nondegenerate periodic lines thus formed are generically partitioned into elliptic and hyperbolic segments that connect through isolated parabolic points (Fig. 1). This means resonances typically occur at both ends of families of tubes and suggests the RIM of tubes and shells may be a universal phenomenon for this class of one-action maps.

The inherently nonresonant nature of chaotic intrasurface dynamics promotes adherence to the averaging principle and thus the survival of (sections of) the invariant surfaces as adiabatic shells. The key to this survival are chaotic regions on the invariant surfaces large enough to admit sufficiently random tracer motion. The invariant surfaces of the outer-topology and intermediate-topology regions meet this condition and thus survive (save the "openings" in the outer-topology region); the invariant surfaces of the inner-topology region host only highly restricted chaotic regions and thus survive only as disconnected segments separated by "leaky"

regions. Thus the survival of the invariant surfaces is strongly connected with the intrasurface dynamics.

Large departures from the noninertial limit destroy the adiabatic state and the topology becomes dominated by an isolated period-1 point and its manifold pair. This topology admits unrestricted chaotic advection and thus constitutes the zero-action state of the system. Zero-action maps in convex domains (as that considered here) invariably accommodate period-1 points and corresponding manifold-pairs, suggesting the topology of the generic case is essentially similar to that of the zero-action state here. Moreover, both one-action and two-action maps collapse on such a zero-action state for sufficiently strong perturbations. Though less clear for nonconvex domains, in general a topology consisting of periodic lines and points and corresponding manifolds is to be expected.[39]

ACKNOWLEDGMENTS

One of the authors (M.F.M.S.) gratefully acknowledges financial support from the Dutch Foundation for Fundamental Research on Matter (FOM). The work presented here has benefitted greatly from numerous scientific discussions with Professor V. V. Meleshko from Kiev National Taras Shevchenko University, Ukraine.

[1] P. B. Kelemen and E. Aharonov, "Periodic formation of magma fractures and generation of layered gabbros in the lower crust beneath oceanic spreading ridges," in *Faulting and Magmatism at Mid-Ocean Ridges*, Geophysical Monograph No. 106, edited by W. R. Buck, P. T. Delaney, J. A. Karson, and Y. Lagabrielle (American Geophysical Union, Washington, D.C., 1998), p. 267.

[2] N. Harnby, M. F. Edwards, and A. W. Nienow, *Mixing in the Process Industries* (Butterworth-Heinemann, Oxford, 1992).

[3] H. Aref, "Chaotic advection in perspective," Chaos, Solitons Fractals **4**, 745 (1994).

[4] G. King, "Towards a science of mixing," Phys. World **11** (11), 23 (1998).

[5] J. M. Ottino, "Mixing, chaotic advection and turbulence," Annu. Rev. Fluid Mech. **22**, 207 (1990).

[6] J. H. E. Cartwright, M. Feingold, and O. Piro, "Chaotic advection in three-dimensional unsteady incompressible laminar flow," J. Fluid Mech. **316**, 259 (1996).

[7] In three-action maps, tracer motion is fully restricted, implying rigid-body fluid motion rather than actual fluid flow. This case thus is of little practical relevance and therefore left out of consideration.

[8] J. H. E. Cartwright, M. Feingold, and O. Piro, "Global diffusion in a realistic three-dimensional time-dependent non-turbulent fluid flow," Phys. Rev. Lett. **75**, 3669 (1995).

[9] I. Mezić, "Break-up of invariant surfaces in action-angle-angle maps and flows," Physica D **154**, 51 (2001).

[10] T. H. Solomon and I. Mezić, "Uniform resonant chaotic mixing in fluid flows," Nature (London) **425**, 376 (2003).

[11] M. Feingold, L. P. Kadanoff, and O. Piro, "A way to connect fluid dynamics to dynamical systems: passive scalars," in *Fractal Aspects of Materials: Disordered Systems*, edited by A. J. Hurd, D. A. Weitz, and B. B. Mandelbrot (Materials Research Society, Warrendale, PA, 1987), p. 203.

[12] M. Feingold, L. P. Kadanoff, and O. Piro, "Passive scalars, three-dimensional volume-preserving maps and chaos," J. Stat. Phys. **50**, 529 (1988).

[13] C. Q. Cheng and Y. S. Sun, "Existence of invariant tori in three-dimensional measure preserving mappings," Celest. Mech. Dyn. Astron. **47**, 275 (1989).

[14] E. Ott, *Chaos in Dynamical Systems* (Cambridge University Press, Cambridge, 1993).

[15] A. Gómez and J. D. Meiss, "Volume-preserving maps with an invariant," Chaos **12**, 289 (2002).

[16] M. F. M. Speetjens, H. J. H. Clercx, and G. J. F. van Heijst, "A numerical and experimental study on advection in three-dimensional Stokes flows," J. Fluid Mech. **514**, 77 (2004).

[17] This is a typical value that may be changed without loss of generality of the discussion hereafter.

[18] M. F. M. Speetjens and H. J. H. Clercx, "A spectral solver for the Navier-Stokes equations in velocity-vorticity formulation," Int. J. Comput. Fluid Dyn. **19**, 191 (2005).

[19] M. F. M. Speetjens, "Three-dimensional chaotic advection in a cylindrical domain," Ph.D. thesis, Eindhoven University of Technology (2001).

[20] V. S. Malyuga, V. V. Meleshko, M. F. M. Speetjens, H. J. H. Clercx, and G. J. F. van Heijst, "Mixing in the Stokes flow in a cylindrical container," Proc. R. Soc. London, Ser. A **458**, 1867 (2002).

[21] K. Bajer, "Hamiltonian formulation of the equations of streamlines in three-dimensional steady flows," Chaos, Solitons Fractals **4**, 895 (1994).

[22] The typification of period-p points $\boldsymbol{x}_{k+p}=\boldsymbol{x}_k$ is based upon local linearization of the map $\boldsymbol{\Phi}_T$. This gives $d\boldsymbol{x}_{k+p}=\boldsymbol{F}\cdot d\boldsymbol{x}_k$, with $d\boldsymbol{x}$ the position in the local frame of reference centered on the periodic point and $\boldsymbol{F}=\partial\boldsymbol{\Phi}_T^p/\partial\boldsymbol{x}|_{\boldsymbol{x}_k}$ the so-called deformation tensor that describes the local deformation of fluid parcels. The eigenvalue spectrum $\boldsymbol{\lambda}=(\lambda_1,\lambda_2,\lambda_3)$ of $\boldsymbol{F}$, with $\lambda_1\lambda_2\lambda_3=1$ due to $\nabla\cdot\boldsymbol{v}=0$, determines the local deformation behavior and enables classification of isolated periodic points and (segments of) periodic lines following Malyuga *et al.* (Ref. 20). Four nondegenerate cases may be distinguished: (i) focus-type isolated point: $\boldsymbol{\lambda}=(\lambda,\exp(i\phi)/\sqrt{\lambda},\exp(-i\phi)/\sqrt{\lambda})$; (ii) node-type isolated point: $(\lambda_1,\lambda_2,(\lambda_1\lambda_2)^{-1})$; (iii) elliptic point on periodic line: $\boldsymbol{\lambda}=(1,\exp(i\phi),\exp(-i\phi))$; (iv) hyperbolic point on periodic line $\boldsymbol{\lambda}=(1,\lambda,\lambda^{-1})$. The degenerate case $\boldsymbol{\lambda}=(1,1,1)$ corresponds with a parabolic point.

[23] These topological features are given in Malyuga *et al.* (Ref. 20) and Speetjens *et al.* (Ref. 16). Note the quantitative difference in translation velocity of the bottom wall results in minor quantitative differences with those for the present configuration. Note furthermore that top and bottom walls are exchanged in Malyuga *et al.*

[24] The time-reversal reflectional symmetry S_1 implies the flow *must* have a period-1 line and *may* have higher-order periodic lines in $\mathcal{S}$. Moreover, period-p lines $\mathcal{L}$ come in clusters $[\mathcal{L},\boldsymbol{\Phi}(\mathcal{L}),\ldots,\boldsymbol{\Phi}^{p-1}(\mathcal{L})]$, meaning the existence of such a line in $\mathcal{S}$ implies a family of lines symmetrically arranged about $\mathcal{S}$.

[25] I. Mezić and S. Wiggins, "On the integrability and perturbation of three-dimensional fluid flows with symmetry," J. Nonlinear Sci. **4**, 157 (1994).

[26] Here the box-counting dimension has been utilized (Ref. 14).

[27] This is essentially similar to the coalescence of invariant curves into surfaces in two-action maps under arbitrarily small perturbations (Ref. 6).

[28] The global topology is in this regime shaped primarily by the period-1 structures; the period-2 structures are therefore left out of consideration here.

[29] V. I. Arnol'd, *Mathematical Methods of Classical Mechanics* (Springer, New York, 1978).

[30] In fact the averaging principle underlying adiabatic approximations itself is "loose" in the sense that it is a strictly untrue but nonetheless fruitful concept that leans on "loose" physical considerations rather than on rigorous mathematical foundations (Ref. 29).

[31] The tubes are complete; resonance-induced dispersion does not occur here.

[32] This reasoning may suggest that elliptic and hyperbolic periodic points give rise to resonance—and thus local defects—as well. However, tracers near hyperbolic points are progressively transported away into the adiabatic shell by the associated manifolds in an essentially nonresonant fashion, leaving the shell intact. Similarly, tracers near elliptic points are transported away through the associated tubes.

[33] R. S. MacKay, J. D. Meiss, and I. C. Percival, "Stochasticity and transport in Hamiltonian systems," Phys. Rev. Lett. **52**, 697 (1984).

[34] Mass conservation implies $A_{\mathcal{A}}\sim T_{\mathcal{A}}\phi_{\mathcal{P}}$, with $A_{\mathcal{A}}$ the area of the shell, $\phi_{\mathcal{P}}$ the flow rate through the tube surface, and $T_{\mathcal{A}}$ the typical time required to drain the shell, or equivalently, the typical residence time of a tracer on the shell. Given $A_{\mathcal{A}}\sim L_{\mathcal{A}}^2$ and $\phi_{\mathcal{P}}\sim L_{\mathcal{P}}V_{\mathcal{P}}$, with $V_{\mathcal{P}}$, the typical transport velocity through the tube and $L_{\mathcal{P}}$ and $L_{\mathcal{A}}$ typical diameters of tube and shell, respectively, and $V_{\mathcal{P}}\sim L_{\mathcal{P}}/T_{\mathcal{P}}$, with $T_{\mathcal{P}}$, the typical residence time of a tracer in the tube, readily leads to $T_{\mathcal{A}}/T_{\mathcal{P}}\sim(L_{\mathcal{A}}/L_{\mathcal{P}})^2$.

[35] The one-directional tracer transport from the inner to outer shell implies continuous drainage of the inner shell and thus may suggest violation of mass conservation at some point in time. However, the adiabatic topology has a very long but nonetheless finite lifespan in the order of 20 000 periods. [This limited durability is inherent in the adiabatic approximation (Ref. 36).] Beyond this timespan, expansion becomes significant and

shells dissolve, admitting an influx of tracers into the regions of dissolving inner shells and thus balancing their drainage during the lifespan of the adiabatic topology.
[36]E. Ott, "Goodness of ergodic adiabatic invariants," Phys. Rev. Lett. **42**, 1628 (1979).
[37]J. M. Ottino, *The Kinematics of Mixing: Stretching, Chaos and Transport* (Cambridge University Press, Cambridge, 1989).
[38]L. E. J. Brouwer, "Über Abbildung von Mannigfaltigkeiten," Math. Ann. **71**, 97 (1911).
[39]D. Beigie, A. Leonard, and S. Wiggins, "Invariant manifold template for chaotic advection," Chaos, Solitons Fractals **4**, 749 (1994).